

Quantum logical controlled-NOT gate in a lithium niobate-on-insulator photonic quantum walk

Robert J. Chapman,^{1,*} Samuel Häusler,² Giovanni Finco,¹ Fabian Kaufmann,¹ and Rachel Grange¹

¹*Optical Nanomaterial Group, Institute for Quantum Electronics,
Department of Physics, ETH Zurich, CH-8093 Zurich, Switzerland*

²*Institute for Sensors and Electronics, University of Applied Sciences
and Arts Northwestern Switzerland, CH-5210 Windisch, Switzerland*

(Dated: May 29, 2023)

Quantum computers comprise elementary logic gates that initialize, control and measure delicate quantum states. One of the most important gates is the controlled-NOT, which is widely used to prepare two-qubit entangled states. The controlled-NOT gate for single photon qubits is normally realized as a six-mode network of individual beamsplitters. This architecture however, utilizes only a small fraction of the circuit for the quantum operation with the majority of the footprint dedicated to routing waveguides. Quantum walks are an alternative photonics platform that use arrays of coupled waveguides with a continuous interaction region instead of discrete gates. While quantum walks have been successful for investigating condensed matter physics, applying the multi-mode interference for logical quantum operations is yet to be shown. Here, we experimentally demonstrate a two-qubit controlled-NOT gate in an array of lithium niobate-on-insulator waveguides. We engineer the tight-binding Hamiltonian of the six evanescently-coupled single-mode waveguides such that the multi-mode interference corresponds to the linear optical controlled-NOT unitary. We measure the two-qubit transfer matrix with 0.938 ± 0.003 fidelity, and we use the gate to generate entangled qubits with 0.945 ± 0.002 fidelity by preparing the control photon in a superposition state. Our results highlight a new application for quantum walks that use a compact multi-mode interaction region to realize large multi-component quantum circuits.

Photonic quantum information technologies use controlled superposition and entangled single photon qubits for applications in quantum computing [1, 2], simulation [3], communication [4] and sensing [5]. At the core of any quantum information processor is the ability to entangle qubits via logical operation such as the controlled-NOT (CNOT) gate, which is fundamental to many leading quantum computing algorithms. These operations are typically the most challenging to perform, as the qubits must interact with each other but be otherwise fully isolated to preserve coherence [6]. In linear optical quantum computing, photonic qubits are entangled by quantum interference at beamsplitters and single photon detection, either in post-selection or by heralding ancillary photons [7]. The typical linear optical CNOT gate is realized in a six-mode interferometer comprising five beamsplitters [8] and has been demonstrated in free-space optics with polarization encoding [9], and in integrated photonics with path encoding [10]. Four modes are for the two qubits and the extra modes provide loss channels that are necessary to balance the probabilistic logical operation. The need for high-fidelity entangling gates puts stringent requirements on the accuracy of the beamsplitter reflectivities, stability of the interferometer and indistinguishability of the single photons in all degrees of freedom. Photonic integrated circuits benefit from the precision and inherent phase stability of monolithic nanofabricated devices, and comprise optical waveguides for routing light on-chip, directional couplers

(DCs) or multi-mode interferometers that act as two-mode beamsplitters, and thermo- or electro-optic phase control for reconfigurability. It is known that a nest of two-mode interferometers can be configured for any linear optical unitary, including the CNOT gate, however, this architecture is dominated by routing of light between separate beamsplitters, which does not contribute to the logical operation [11, 12].

Quantum walks (QWs) are an alternative photonics architecture, realized as arrays of coupled waveguides where light interferes along the entire propagation length instead of at individual beamsplitters. The optical evolution in the QW is described by a tight-binding Hamiltonian that can be engineered for many applications and for studying fundamental physics. This includes the experimental demonstration of topologically bound states [13–18], Anderson localization [19–23], quantum transport [24, 25] and for preparing large single photon superposition states [26]. When pairs of indistinguishable photons propagate in a QW, they undergo bosonic bunching similar to the Hong-Ou-Mandel (HOM) effect, which has been observed in free-space optics [27], multi-mode fiber-optics [28] and integrated photonics [29]. It has been recently proposed that multi-mode quantum interference in a specifically parameterized six-waveguide array can implement the CNOT gate on path-encoded photonic qubits [30]. In this realization of the CNOT gate, the photons interfere continuously along the length of the array, removing the need for on-chip routing. However, such a device is challenging to produce because of the precise control required on the tight-binding Hamiltonian for each propagation and hopping term. While sophisti-

* rchapman@ethz.ch

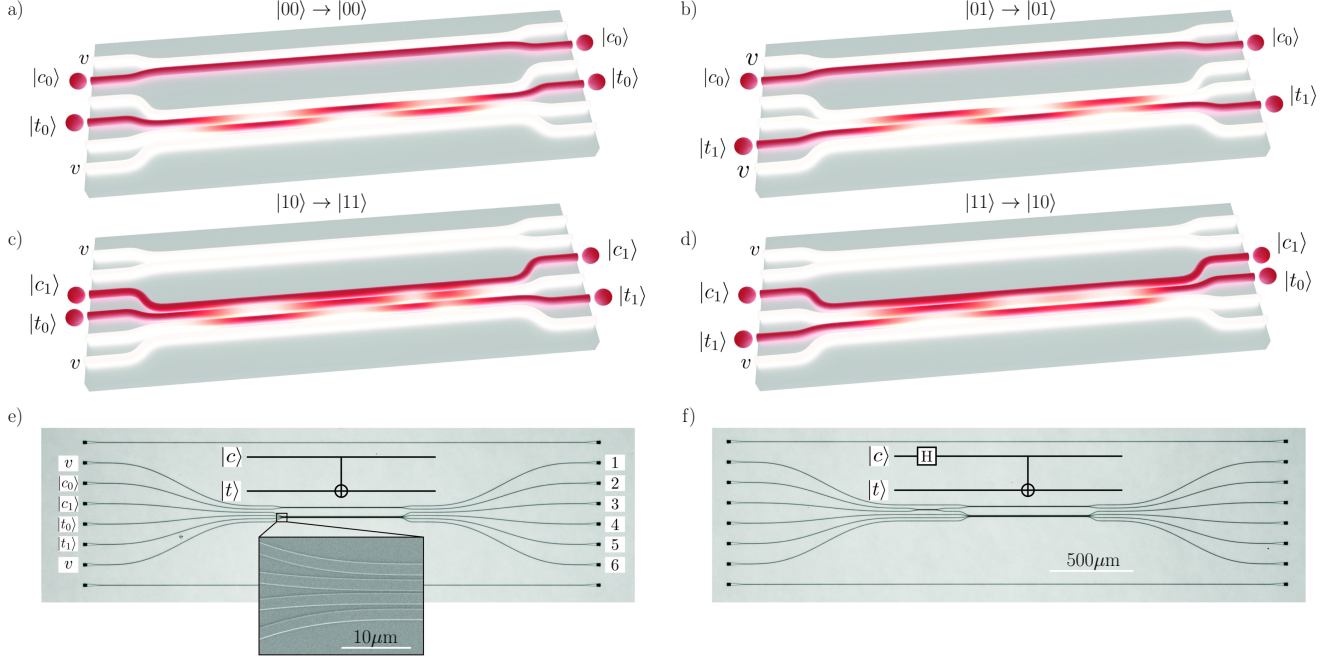


Figure 1. Evolution of the QW-CNOT device. Two-qubit evolution in the QW-CNOT waveguide array shown in the two-qubit logical subspace for input states $|ct\rangle$: a) $|00\rangle$, b) $|01\rangle$, c) $|10\rangle$, and d) $|11\rangle$. Labels $|c\rangle$ and $|t\rangle$ indicate the control and target qubits, and the input waveguides labeled v are auxiliary modes. When the control qubit is in the $|1\rangle$ state the photon interferes with the target qubit and causes a bit-flip operation. This operation is only possible when post-selecting the logical subspace. e) A microscope image of the QW-CNOT realized in the LNOI photonics platform. The labels on the left show the qubit encoding and on the right the waveguide number. The inset shows a scanning electron micrograph of the start of the coupling region. f) A microscope image of the QW-CNOT array with an additional DC that implements a Hadamard gate, labeled H, preparing the control qubit in a superposition state.

cated QWs have been demonstrated in several photonics technologies, controlled two-qubit gates are yet to be realized.

Here, we experimentally demonstrate the two-qubit CNOT gate realized in a continuous time QW. We fabricated the six-waveguide “QW-CNOT” array in lithium niobate-on-insulator (LNOI) and fully control the on-site energies and nearest-neighbor hopping of the tight-binding Hamiltonian in the design of the individual waveguide widths and separations respectively. We measure the two-qubit CNOT transfer matrix with a fidelity of 0.938 ± 0.003 using photons generated by spontaneous parametric down-conversion (SPDC). The reduced fidelity is due to the limited indistinguishability of the SPDC source, bandwidth of the QW-CNOT chip and fiber dispersion. We also prepare the control qubit in the $\frac{1}{\sqrt{2}}(|0\rangle + e^{i\phi}|1\rangle)$ superposition state using an on-chip directional coupler and use the QW-CNOT gate to generate the state $\frac{1}{\sqrt{2}}(|00\rangle + e^{i\phi}|11\rangle)$ with fidelity 0.945 ± 0.002 , measured in the computational basis. The addition of on-chip phase control would enable generation of maximally entangled Bell states, which are an important resource for quantum computing and quantum communication. Our results open a pathway towards implementing large multi-mode photonic circuits in a single step using QWs.

RESULTS

Quantum controlled-NOT gate in a photonic quantum walk

The quantum walk controlled-NOT (QW-CNOT) gate operates on path encoded control $|c\rangle$ and target $|t\rangle$ qubits, that are superposition states of photon occupation across pairs of neighboring waveguides. The evolution of the quantum walk is described by the tight-binding Hamiltonian

$$h = \sum_{i=1}^N \beta_i \hat{a}_i^\dagger \hat{a}_i + \sum_{i=1}^{N-1} \kappa_i \left(\hat{a}_i^\dagger \hat{a}_{i+1} + \hat{a}_{i+1}^\dagger \hat{a}_i \right), \quad (1)$$

which is the sum of the propagation coefficients of each waveguide $\beta_i = 2\pi n_{\text{eff},i}/\lambda$ and the coupling rates between neighboring waveguides κ_i . The unitary operation is described by Schrödinger’s equation $U = \exp(-iht)$ for an evolution time t . Lahini *et al.* determined the specific six waveguide tight-binding Hamiltonian with an equivalent unitary to the traditional linear optical CNOT gate [30], which is usually realized as a network of five beam-splitters [8] (shown in Supplementary Section 1). The

QW-CNOT requires the Hamiltonian-time product

$$ht = \pi \begin{pmatrix} 0 & -1.27 & 0 & 0 & 0 & 0 \\ -1.27 & -0.73 & 0 & 0 & 0 & 0 \\ 0 & 0 & 0.67 & -0.51 & 0 & 0 \\ 0 & 0 & -0.51 & 0.01 & -1.69 & 0 \\ 0 & 0 & 0 & -1.69 & -1.01 & -0.52 \\ 0 & 0 & 0 & 0 & -0.52 & -1.67 \end{pmatrix}, \quad (2)$$

where diagonal terms correspond to the propagation coefficients β_i and the off-diagonal terms correspond to the nearest-neighbor hopping rates κ_i . The two-photon evolution for each input state is shown in Figure 1 for the reduced logical subspace. Four waveguides are required to encode the two qubits and two additional auxiliary modes that allow the photons to propagate in a larger Hilbert space that is subsequently reduced by post-selection. Figures 1a and 1b show the control qubit in the $|0\rangle$ state where it is decoupled from the rest of the array and does not interfere with the target qubit. Coupling to the auxiliary modes and to other non-logical modes are not shown in this evolution, but can be seen in the complete Hilbert space (shown in Supplementary Section 2). Figures 1c and 1d show the control qubit in the $|1\rangle$ state, where it quantum interferes with the target qubit. Quantum interference between the two photons leads to a bit-flip operation on the target qubit. The visualization here does not consider the amplitude of the state within the two-qubit subspace where each of the logical transformations has a $1/9$ success probability (shown in Supplementary Section 2).

QW-CNOT design and fabrication

We use the lithium niobate-on-insulator (LNOI) photonics platform to implement a QW-CNOT gate with waveguides designed for 1550 nm wavelength and transverse electric polarization. LNOI has a broad transparency range, low loss, and high electro-optic and $\chi^{(2)}$ nonlinear coefficients, making it a leading technology for photonic quantum information processors [31]. LNOI has become a major focus in photonics research, with demonstrations of record high-speed and low-voltage modulation [32], ultra-efficient nonlinear frequency conversion [33], all-optical switching [34] and entangled photon pair generation [35]. We etch the waveguide array in a 300 nm LN film with a 4.7 μm SiO_2 bottom oxide on a silicon handle wafer [36]. The etched waveguide height is 230 nm and we use the width and separation to control the propagation coefficients β_i and coupling rates κ_i in the tight-binding Hamiltonian. We initially simulate the mode for various waveguide widths using a finite-element solver and plot the corresponding β terms in Figure 2a. The inset in Figure 2a shows the typical waveguide cross section and solution of the fundamental transverse electric mode. We exchange time-evolution for equivalent length-evolution for designing the array and target an array

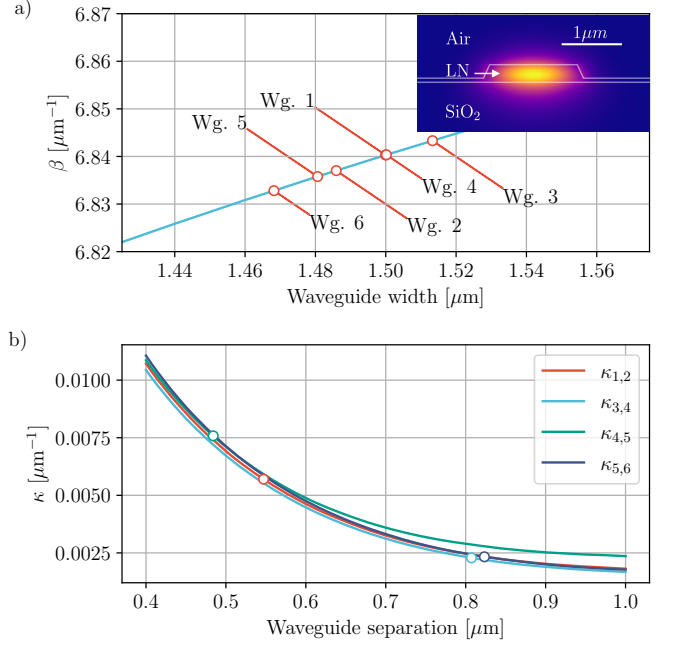


Figure 2. Design of the QW-CNOT array in LNOI photonics. a) The dependence of the propagation coefficient β on the waveguide width (top edge) with a fixed etch depth of 230 nm and remaining film of 70 nm. The required waveguide widths are indicated on the curve. The inset shows the fundamental transverse electric mode of the LNOI waveguide. b) The dependence of the coupling coefficient κ on the waveguide separation (edge to edge) for each of the coupled waveguides. Waveguides 2 and 3 are not coupled as $\kappa_2 = 0$ in the Hamiltonian.

length $L = 700 \mu\text{m}$ such that the Hamiltonian-length product $\hbar L$ matches Equation 2. We chose the on-site terms to be relative about the first waveguide which we set to $1.5 \mu\text{m}$ width and indicate the necessary propagation coefficients as points in Figure 2a. Using the determined waveguide widths, we simulate the even and odd supermodes of neighboring waveguides to calculate the coupling rate as $\kappa = \pi(n_{\text{even}} - n_{\text{odd}})/\lambda$, as shown in Figure 2b. The points indicate the necessary parameters for the Hamiltonian. Note that there is no hopping between waveguides 2 and 3 in the Hamiltonian as $\kappa_2 = 0$. The waveguide numbering is shown in Figure 1e, and we position waveguides 2 and 3 with a $20 \mu\text{m}$ gap to effectively decouple the modes. Figure 1e shows a microscope image of the QW-CNOT and Figure 1f shows another device on the same chip with an additional DC that prepares the control qubit in a superposition state. The different waveguide separations can be seen in the scanning electron micrograph and reflects the different coupling coefficients of the Hamiltonian. We couple light to the chip using grating couplers with ~ 6 dB loss per coupler. Grating couplers offer several advantages over end-fire coupling, such as eliminating the need for dicing and polishing waveguide facets, larger mode field diameters, and polarization sensitivity, ensuring the excitation

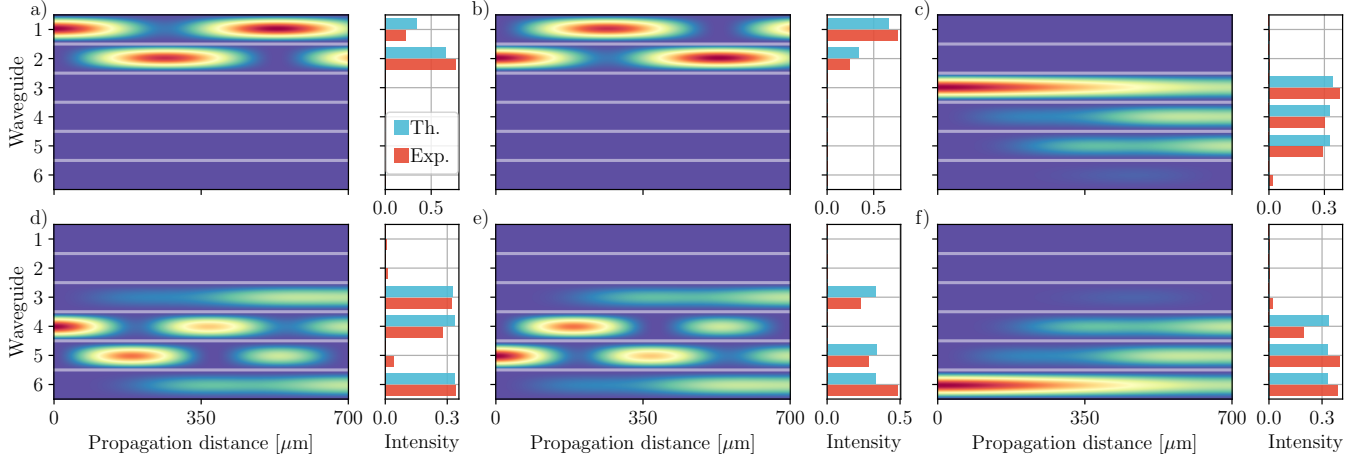


Figure 3. **Classical characterization.** The theoretical evolution intensity in the QW-CNOT chip for each of the six waveguide inputs. The output intensity for each evolution is shown for the theoretical model (blue) and the experimental result (red). The theoretical evolution is calculated from the Hamiltonian in Equation 1 with the values of β and κ shown in Figure 2.

of only the waveguide transverse electric mode. Higher efficiency grating couplers in LNOI have been reported [37–39] with losses as low as <1 dB per grating [40].

Classical characterization

To classically characterize the QW-CNOT gate, we inject a 1550 nm wavelength continuous-wave laser into each input of the chip and record the intensity at all the outputs with a near-infrared camera. Figure 3 shows the propagation simulation based on the Hamiltonian in Equation 2, as well as measured output intensity distributions for each of the six inputs in the waveguide array. The propagation here differs from the two-photon evolution shown in Figure 1 as only a single mode is excited. We calculate the fidelity between the experimental transfer matrix Γ and the theoretical transfer matrix Γ' as

$$F(\Gamma, \Gamma') = \sum_{i,j} \sqrt{\frac{\Gamma_{i,j} \Gamma'_{i,j}}{(\sum_{i,j} \Gamma_{i,j}) (\sum_{i,j} \Gamma'_{i,j})}}. \quad (3)$$

The fidelity between the classically characterized transfer matrix and the theoretical model is 0.982 ± 0.007 where the error is calculated from the variation in fidelity for each waveguide input. From this characterization, we can build a simulation of the device by finding the Hamiltonian that gives the closest match to the measured output. This simulation will be a tool for predicting the two-photon dynamics of the QW-CNOT chip.

SPDC source and experimental setup

In order to measure the two-qubit operation of the QW-CNOT gate, we require a source of indistinguishable photons at 1550 nm wavelength. To achieve this, we

employ a collinear type-2 spontaneous parametric down-conversion (SPDC) process using a beta-barium borate crystal. A diagram of the complete experimental setup is depicted in Figure 4. We use a 775 nm continuous-wave laser to pump the nonlinear crystal, generating photon pairs which are filtered with a 12 nm bandpass filter to ensure both photons have the same bandwidth. Because we use a type-2 SPDC process, one photon is horizontally polarized and the other vertically polarized. We couple both photons into a polarization maintaining fiber and separate them with a fiber-pigtailed polarizing beamsplitter. One of the output fibers is pigtailed with the slow axis vertical and the other fiber with the slow axis horizontal, so that both photons exit the beamsplitter with the same polarization in each fiber. Motor-controlled optical delay lines compensate for mismatch in fiber lengths and birefringence before the photons are coupled to the chip. Photons are coupled to and from the chip with fiber arrays positioned above the grating couplers with precision translation stages. Finally, coincidence measurements are performed with superconducting nanowire single photon detectors and a time correlator to record arrival times. We verify the indistinguishability of the generated photons through the characteristic HOM dip, measured by interfering the photons in a fused-silica 50:50 beamsplitter with 94.6 % visibility (further details in Supplementary Section 3). Narrower bandpass filters can improve the source visibility by reducing fiber dispersion at the cost of lowering the photon count rate.

QW-CNOT array two-qubit transfer matrix

The operation of the two-qubit QW-CNOT chip is based on quantum interference between the control and target qubits. The control $|0\rangle$ state does not interfere with the target qubit and thus the arrival time of the

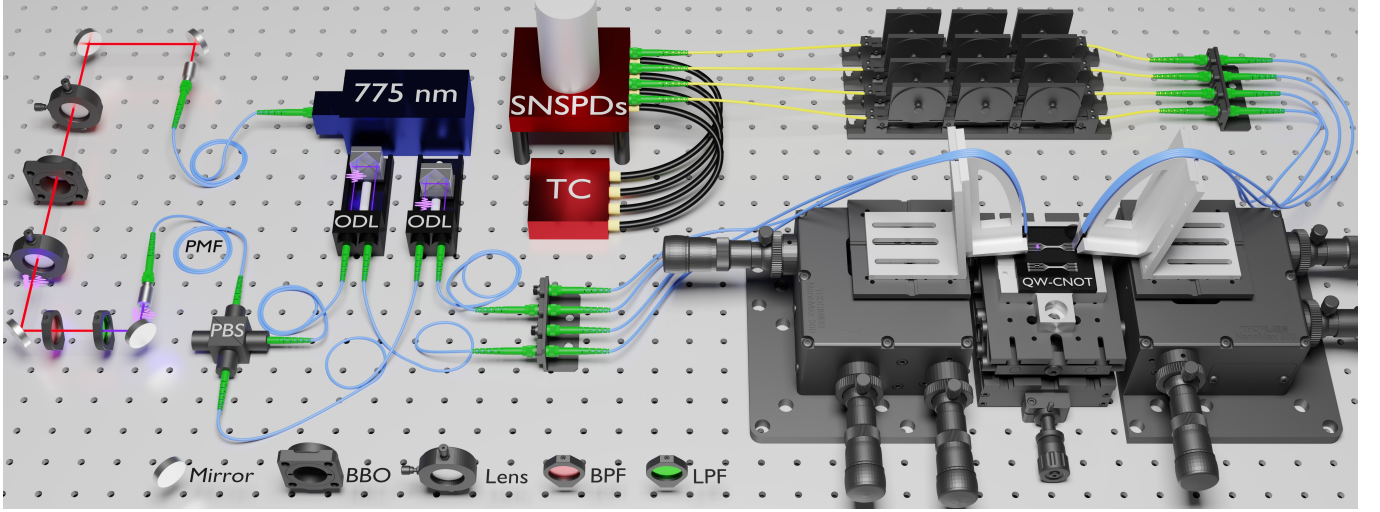


Figure 4. **Experimental setup.** Orthogonally polarized photon-pairs are generated by type-2 spontaneous parametric down-conversion in a 2 mm-thick beta barium borate (BBO) crystal and the pump is filtered with a longpass filter (LPF) and the photons with a 12 nm bandpass filter (BPF). The photons are coupled to polarization maintaining fiber (PMF) and separated with a polarizing beamsplitter (PBS) where one fiber pigtail is rotated such that both photons have the same output polarization. The photons are injected into optical delay lines (ODLs) to compensate for fiber length mismatch and fiber birefringence and are coupled to the QW-CNOT chip with a fiber array positioned above on-chip grating couplers. After the quantum walk, the photons are collected in fiber and measured with superconducting nanowire single photon detectors (SNSPDs) and the arrival times are recorded with a time correlator (TC). Polarization controllers are used to maximize the efficiency of the SNSPDs.

two photons has no impact on the transfer matrix. However, for the control $|1\rangle$ state, the photon arrival times are critical to allow for interference. We use the motorized optical delay lines to match the arrival times of the control and target qubits. For the input state $|10\rangle$, we observe HOM interference between waveguides 3 and 4, which results in suppression of the output state $|10\rangle$ and therefore only the logical output $|11\rangle$ is measured. Likewise for input state $|11\rangle$, HOM interference is observed between waveguides 3 and 5, meaning only the logical output $|10\rangle$ is measured. This interference gives rise to the logical CNOT operation in our chip. The raw HOM interference plots are shown in Supplementary Section 4. We measure the two-qubit transfer matrix of the QW-CNOT chip with and without a delay between the photons and plot the results in Figure 5. When the photons arrive at the chip with a time delay (τ), there is no quantum interference and we observe classical propagation dynamics. In Figures 5a, 5b and 5c, we show the ideal theoretical, simulation and experimental results respectively. Because there is no quantum interference, the simulation is simply the product of the classical probability distributions shown in Figure 3. We calculate the fidelity using Equation 3 between the theoretical model and the experiment as 0.994 ± 0.001 and between the simulation and the experiment as 0.991 ± 0.001 , where errors are calculated using Poissonian statistics.

We scan the optical delay lines and measure HOM interference between the control and target photons in the QW-CNOT waveguide array. When the delay is $\tau = 0$, the photons arrive simultaneously and the CNOT opera-

tion is implemented by quantum interference. The theoretical, simulated and experimentally measured transfer matrices are shown in Figures 5d, 5e and 5f respectively. The fidelity between the theoretical model and the experiment is 0.938 ± 0.003 and between the simulation and the experiment is 0.985 ± 0.002 . The reduced fidelity of the two-photon interference is attributed to the relatively broad bandwidth of the SPDC photons (12 nm), meaning optical dispersion in fibers and waveguide, and the sensitivity of the Hamiltonian to wavelength, decrease the visibility of the two-qubit interference.

Entangled state generation

The CNOT gate is a fundamental element for quantum computation and can be used to prepare maximally entangled Bell states when the control qubit is in the superposition state $|c\rangle = \frac{1}{\sqrt{2}}(|0\rangle \pm |1\rangle)$ and the target qubit in either the $|0\rangle$ or $|1\rangle$ state. We fabricated a QW-CNOT gate with the addition of a DC that prepares the control qubit in the superposition state $|c\rangle = \frac{1}{\sqrt{2}}(|0\rangle + e^{i\phi}|1\rangle)$ and the target qubit is kept in the $|0\rangle$ state. We do not control the phase ϕ in this experiment, however, the addition of electro-optic or thermo-optic phase shifters [41] would enable the control necessary to prepare maximally entangled Bell states. When the two photons arrive with a time delay τ , the input state becomes an incoherent mixture $\frac{1}{2}(|00\rangle\langle 00| + |10\rangle\langle 10|)$ and no quantum interference is observed. The expected output of the QW-CNOT in this case is $\frac{1}{4}(|00\rangle\langle 00| + 2|10\rangle\langle 10| + |11\rangle\langle 11|)$. On

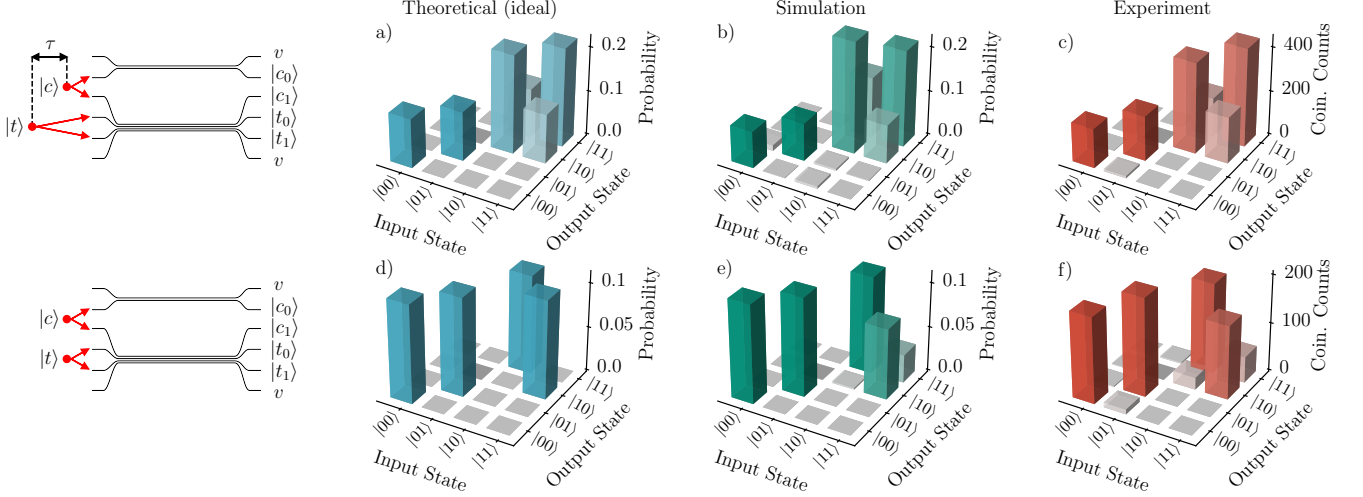


Figure 5. **Two-qubit transfer matrix.** a, b, c) The theoretical (ideal), simulated and experimental two-qubit transfer matrix when the photons arrive with a time separation τ . In this regime, the photons do not quantum interfere. d, e, f) The theoretical (ideal), simulated and experimental two-qubit transfer matrix with indistinguishable photons that arrive with zero time delay.

the other hand, when the photons arrive simultaneously, i.e $\tau = 0$, the input state is a coherent superposition $\frac{1}{\sqrt{2}}(|00\rangle + e^{i\phi}|10\rangle)$ and the expected output is the entangled state $\frac{1}{\sqrt{2}}(|00\rangle + e^{i\phi}|11\rangle)$. The entangled state preparation results are presented in Figure 6. Based on the two-photon transfer matrix measured previously, we construct a model of the two-qubit entangled state preparation. The theoretical, simulated and measured output for the incoherent input state, measured in the computational basis, are shown in Figures 6a, 6b, and 6c respectively. We calculate the fidelity between the theoretical state and the experiment as 0.985 ± 0.001 and between the simulated state and the experiment as 0.987 ± 0.001 . The theoretical, simulated and measured output for the coherent superposition input state are shown in Figures 6d, 6e, and 6f respectively. The fidelity between the theoretical output and the experiment is 0.945 ± 0.002 and between the simulation and experiment is 0.973 ± 0.001 . Although these results are from a different QW-CNOT device, the experiment and simulation show good agreement. The fidelity here assumes $\phi = 0$, which can be achieved with an on-chip phase shifter for the input control qubit. The two-qubit entangled state could be verified by performing two-qubit state tomography or violating the Clauser, Horn, Shimony and Holt (CHSH) inequality [42]. Nevertheless, this experiment shows the QW-CNOT device is capable of performing photonic entangling gates in a single interaction step, which could provide a significant improvement over the traditional multi-step circuit approach.

DISCUSSION

We have successfully implemented the controlled-NOT gate in a continuous-time quantum walk on the lithium niobate-on-insulator photonics platform. Using indistinguishable photons from a SPDC source, we have measured the transfer matrix of the two-qubit CNOT gate, and prepared the control qubit in a superposition leading to the generation of entangled states. Our demonstration does not yet benefit from the key advantages of LNOI photonics, however, we aim to improve gate fidelity by including electro-optical tuning to locally modify the array Hamiltonian. With enough control, this could also enable us to reconfigure the array for different logical operations and provide a new platform for programmable integrated photonics. Another improvement would come from adding input and output single qubit gates for performing process and state tomography, violating the CHSH inequality and preparing arbitrary two-qubit states. In this work, we highlight the potential for photonic quantum gates to be implemented in continuously coupled waveguide arrays, offering a more compact solution compared to existing architectures and opening new pathways towards the development of more complex multi-photon circuits in a single interaction region.

Data availability

Raw data and evaluation code are available from the authors upon reasonable request.

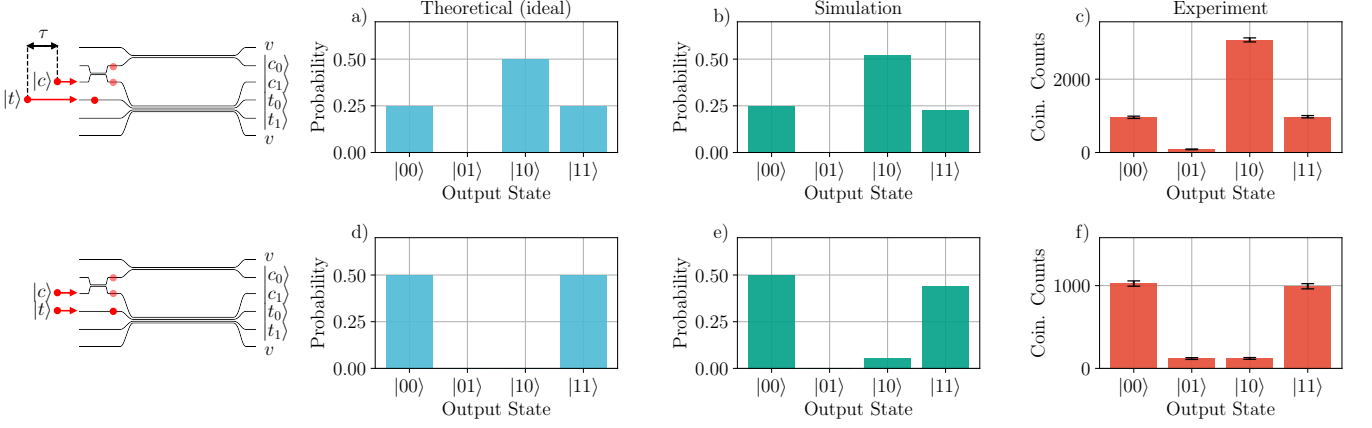


Figure 6. **Entangled state preparation.** A directional coupler is included before the QW-CNOT array to prepare the control qubit in a superposition state $(|0\rangle + e^{i\phi}|1\rangle)/\sqrt{2}$. a, b, c) The theoretical (ideal), simulated and experimental two-qubit output when the photons arrive with a time difference τ . This means the two qubits are distinguishable and no entanglement is generated. d, e, f) The theoretical (ideal), simulated and experimental two-qubit output when the photons arrive together and undergo HOM interference. In this case, the entangled state $(|00\rangle + e^{i\phi}|11\rangle)/\sqrt{2}$ is generated. The error bars in c) and f) are calculated from Poissonian statistics.

Competing interests

manuscript.

The authors declare no competing financial or non-financial interests.

Acknowledgments

We acknowledge support for characterization of our samples from the Scientific Center of Optical and Electron Microscopy ScopeM and from the cleanroom facilities BRNC and FIRST of ETH Zurich and IBM Ruschlikon. R.J.C. acknowledges support from the Swiss National Science Foundation under the Ambizione Fellowship Program (Project Number PZ00P2.208707). R.G. acknowledges support from the European Space Agency (Project Number 4000137426), the Swiss National Science Foundation under the Bridge Program (Project Number 194693), the European Research Council (Project Number 714837), and Horizon 2020 (ELENA Consortium, Project Number 101016138).

Author Contributions

R.J.C. conceived the experiment. R.J.C. and S.H. designed the waveguide array. G.F. and F.K. fabricated the lithium niobate-on-insulator waveguide samples. R.J.C. performed the optical measurements, data analysis and wrote the original draft of the manuscript. R.G. supervised the project. All authors contributed to revising the

-
- [1] J. L. O'Brien, Optical Quantum Computing, *Science* **318**, 1567 (2007).
 - [2] S. Slussarenko and G. J. Pryde, Photonic quantum information processing: A concise review, *Applied Physics Reviews* **6**, 041303 (2019).
 - [3] A. Aspuru-Guzik and P. Walther, Photonic quantum simulators, *Nature Physics* **8**, 285 (2012).
 - [4] N. Gisin and R. Thew, Quantum communication, *Nature Photonics* **1**, 165 (2007).
 - [5] S. Pirandola, B. R. Bardhan, T. Gehring, C. Weedbrook, and S. Lloyd, Advances in photonic quantum sensing, *Nature Photonics* **12**, 724 (2018).
 - [6] T. D. Ladd, F. Jelezko, R. Laflamme, Y. Nakamura, C. Monroe, and J. L. O'Brien, Quantum computers, *Nature* **464**, 45 (2010).
 - [7] E. Knill, R. Laflamme, and G. J. Milburn, A scheme for efficient quantum computation with linear optics, *Nature* **409**, 46 (2001).
 - [8] T. C. Ralph, N. K. Langford, T. B. Bell, and A. G. White, Linear optical controlled-NOT gate in the coincidence basis, *Physical Review A* **65**, 062324 (2002).
 - [9] J. L. O'Brien, G. J. Pryde, A. G. White, T. C. Ralph, and D. Branning, Demonstration of an all-optical quantum controlled-NOT gate, *Nature* **426**, 264 (2003).
 - [10] A. Politi, M. J. Cryan, J. G. Rarity, S. Yu, and J. L. O'Brien, Silica-on-Silicon Waveguide Quantum Circuits, *Science* **320**, 646 (2008).
 - [11] M. Reck, A. Zeilinger, H. J. Bernstein, and P. Bertani, Experimental realization of any discrete unitary operator, *Physical Review Letters* **73**, 58 (1994).

- [12] W. R. Clements, P. C. Humphreys, B. J. Metcalf, W. S. Kolthammer, and I. A. Walmsley, Optimal design for universal multiport interferometers, *Optica* **3**, 1460 (2016).
- [13] Y. E. Kraus, Y. Lahini, Z. Ringel, M. Verbin, and O. Zilberberg, Topological States and Adiabatic Pumping in Quasicrystals, *Physical Review Letters* **109**, 106402 (2012).
- [14] M. Hafezi, S. Mittal, J. Fan, A. Migdall, and J. M. Taylor, Imaging topological edge states in silicon photonics, *Nature Photonics* **7**, 1001 (2013).
- [15] M. C. Rechtsman, J. M. Zeuner, Y. Plotnik, Y. Lumer, D. Podolsky, F. Dreisow, S. Nolte, M. Segev, and A. Szameit, Photonic Floquet topological insulators, *Nature* **496**, 196 (2013).
- [16] S. Mittal, E. A. Goldschmidt, and M. Hafezi, A topological source of quantum light, *Nature* **561**, 502 (2018).
- [17] O. Zilberberg, S. Huang, J. Guglielmon, M. Wang, K. P. Chen, Y. E. Kraus, and M. C. Rechtsman, Photonic topological boundary pumping as a probe of 4D quantum Hall physics, *Nature* **553**, 59 (2018).
- [18] J.-L. Tambasco, G. Corrielli, R. J. Chapman, A. Crespi, O. Zilberberg, R. Osellame, and A. Peruzzo, Quantum interference of topological states of light, *Science Advances* **4**, eaat3187 (2018).
- [19] T. Schwartz, G. Bartal, S. Fishman, and M. Segev, Transport and Anderson localization in disordered two-dimensional photonic lattices, *Nature* **446**, 52 (2007).
- [20] Y. Lahini, A. Avidan, F. Pozzi, M. Sorel, R. Morandotti, D. N. Christodoulides, and Y. Silberberg, Anderson Localization and Nonlinearity in One-Dimensional Disordered Photonic Lattices, *Physical Review Letters* **100**, 013906 (2008).
- [21] L. Martin, G. D. Giuseppe, A. Perez-Leija, R. Keil, F. Dreisow, M. Heinrich, S. Nolte, A. Szameit, A. F. Abouraddy, D. N. Christodoulides, and B. E. A. Saleh, Anderson localization in optical waveguide arrays with off-diagonal coupling disorder, *Optics Express* **19**, 13636 (2011).
- [22] A. Crespi, R. Osellame, R. Ramponi, V. Giovannetti, R. Fazio, L. Sansoni, F. De Nicola, F. Sciarrino, and P. Mataloni, Anderson localization of entangled photons in an integrated quantum walk, *Nature Photonics* **7**, 322 (2013).
- [23] A. Blanco-Redondo, B. Bell, D. Oren, B. J. Eggleton, and M. Segev, Topological protection of biphoton states, *Science* **362**, 568 (2018).
- [24] A. Perez-Leija, R. Keil, A. Kay, H. Moya-Cessa, S. Nolte, L.-C. Kwek, B. M. Rodriguez-Lara, A. Szameit, and D. N. Christodoulides, Coherent quantum transport in photonic lattices, *Physical Review A* **87**, 012309 (2013).
- [25] R. J. Chapman, M. Santandrea, Z. Huang, G. Corrielli, A. Crespi, M.-H. Yung, R. Osellame, and A. Peruzzo, Experimental perfect state transfer of an entangled photonic qubit, *Nature Communications* **7**, 11339 (2016).
- [26] M. Gräfe, R. Heilmann, A. Perez-Leija, R. Keil, F. Dreisow, M. Heinrich, H. Moya-Cessa, S. Nolte, D. N. Christodoulides, and A. Szameit, On-chip generation of high-order single-photon W-states, *Nature Photonics* **8**, 791 (2014).
- [27] A. Schreiber, K. N. Cassemiro, V. Potocek, A. Gabris, P. J. Mosley, E. Andersson, I. Jex, and C. Silberhorn, Photons Walking the Line: A Quantum Walk with Adjustable Coin Operations, *Physical Review Letters* **104**, 050502 (2010).
- [28] H. Defienne, M. Barbieri, I. A. Walmsley, B. J. Smith, and S. Gigan, Two-photon quantum walk in a multimode fiber, *Science Advances* **2**, e1501054 (2016).
- [29] A. Peruzzo, M. Lobino, J. C. F. Matthews, N. Matsuda, A. Politi, K. Poulios, X.-Q. Zhou, Y. Lahini, N. Ismail, K. Wörhoff, Y. Bromberg, Y. Silberberg, M. G. Thompson, and J. L. O'Brien, Quantum Walks of Correlated Photons, *Science* **329**, 1500 (2010).
- [30] Y. Lahini, G. R. Steinbrecher, A. D. Bookatz, and D. Englund, Quantum logic using correlated one-dimensional quantum walks, *npj Quantum Information* **4**, 1 (2018).
- [31] D. Zhu, L. Shao, M. Yu, R. Cheng, B. Desiatov, C. J. Xin, Y. Hu, J. Holzgrafe, S. Ghosh, A. Shams-Ansari, E. Puma, N. Sinclair, C. Reimer, M. Zhang, and M. Lončar, Integrated photonics on thin-film lithium niobate, *Advances in Optics and Photonics* **13**, 242 (2021).
- [32] C. Wang, M. Zhang, X. Chen, M. Bertrand, A. Shams-Ansari, S. Chandrasekhar, P. Winzer, and M. Lončar, Integrated lithium niobate electro-optic modulators operating at CMOS-compatible voltages, *Nature*, 1 (2018).
- [33] J. Lu, J. B. Surya, X. Liu, A. W. Bruch, Z. Gong, Y. Xu, and H. X. Tang, Periodically poled thin-film lithium niobate microring resonators with a second-harmonic generation efficiency of 250,000%/W, *Optica* **6**, 1455 (2019).
- [34] Q. Guo, R. Sekine, L. Ledezma, R. Nehra, D. J. Dean, A. Roy, R. M. Gray, S. Jahani, and A. Marandi, Femtojoule femtosecond all-optical switching in lithium niobate nanophotonics, *Nature Photonics* **16**, 625 (2022).
- [35] J. Zhao, C. Ma, M. Rusing, and S. Mookherjee, High Quality Entangled Photon Pair Generation in Periodically Poled Thin-Film Lithium Niobate Waveguides, *Physical Review Letters* **124**, 163603 (2020).
- [36] F. Kaufmann, G. Finco, A. Maeder, and R. Grange, Redeposition-free inductively-coupled plasma etching of lithium niobate for integrated photonics, *Nanophotonics* 10.1515/nanoph-2022-0676 (2023).
- [37] I. Krasnokutskaya, R. J. Chapman, J.-L. J. Tambasco, and A. Peruzzo, High coupling efficiency grating couplers on lithium niobate on insulator, *Optics Express* **27**, 17681 (2019).
- [38] S. Kang, R. Zhang, Z. Hao, D. Jia, F. Gao, F. Bo, G. Zhang, and J. Xu, High-efficiency chirped grating couplers on lithium niobate on insulator, *Optics Letters* **45**, 6651 (2020).
- [39] E. Lomonte, F. Lenzini, and W. H. P. Pernice, Efficient self-imaging grating couplers on a lithium-niobate-on-insulator platform at near-visible and telecom wavelengths, *Optics Express* **29**, 20205 (2021).
- [40] B. Chen, Z. Ruan, X. Fan, Z. Wang, J. Liu, C. Li, K. Chen, and L. Liu, Low-loss fiber grating coupler on thin film lithium niobate platform, *APL Photonics* **7**, 076103 (2022).
- [41] A. Maeder, F. Kaufmann, D. Pohl, J. Kellner, and R. Grange, High-bandwidth thermo-optic phase shifters for lithium niobate-on-insulator photonic integrated circuits, *Optics Letters* **47**, 4375 (2022).
- [42] J. F. Clauser, M. A. Horne, A. Shimony, and R. A. Holt, Proposed Experiment to Test Local Hidden-Variable Theories, *Physical Review Letters* **23**, 880 (1969).

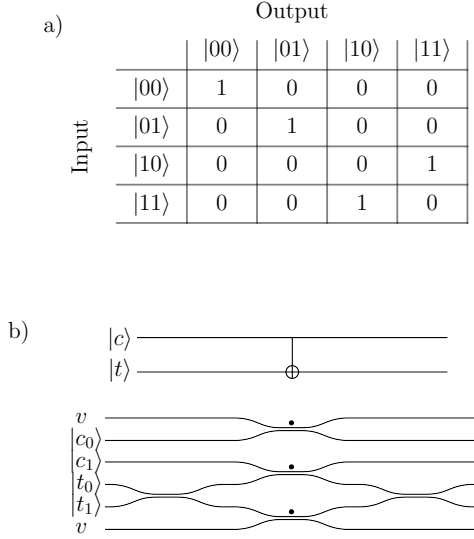


Figure S1. **Controlled-NOT gate.** a) The truth table of the controlled-NOT gate. Input and output states correspond to $|ct\rangle$ where $|c\rangle$ is the control and $|t\rangle$ is the target qubit. b) Linear optical realization based on $1/2$ and $1/3$ (with a dot) beamsplitters. The gate is post-selected on two photons being in the two-qubit logical subspace. The auxiliary modes v are necessary to balance the post-selected logical operation.

SUPPLEMENTARY MATERIAL

1. Linear optical CNOT gate

Figure S1a shows the truth table for the controlled-NOT quantum gate. The state of the target qubit is flipped conditional on the control qubit being in the $|1\rangle$ state. If the control qubit is in a superposition state, the CNOT gate will prepare an entangled two-qubit state. Figure S1b shows the typical post-selected linear optical CNOT gate. The two qubits are labeled $|c\rangle$ and $|t\rangle$ for control and target using standard path encoding. The directional couplers without a dot have reflectivity $1/2$ and with a dot have reflectivity $1/3$. Quantum interference at the central beamsplitter and post-selection lead to generation of entangled states. The auxiliary modes v are necessary to balance the operation, and the gate has a success probability of $1/9$, where the failed operations exit the two-qubit subspace and are therefore not measured.

2. CNOT array design

The evolution of the Hamiltonian-time product in Equation 2 of the main text gives the two-qubit photon CNOT gate operation. The correct logical transformations have a success probability $1/9$ after evolution and are shown in Figure S2a and the other transformations that exit the two-qubit subspace are shown in Fig-

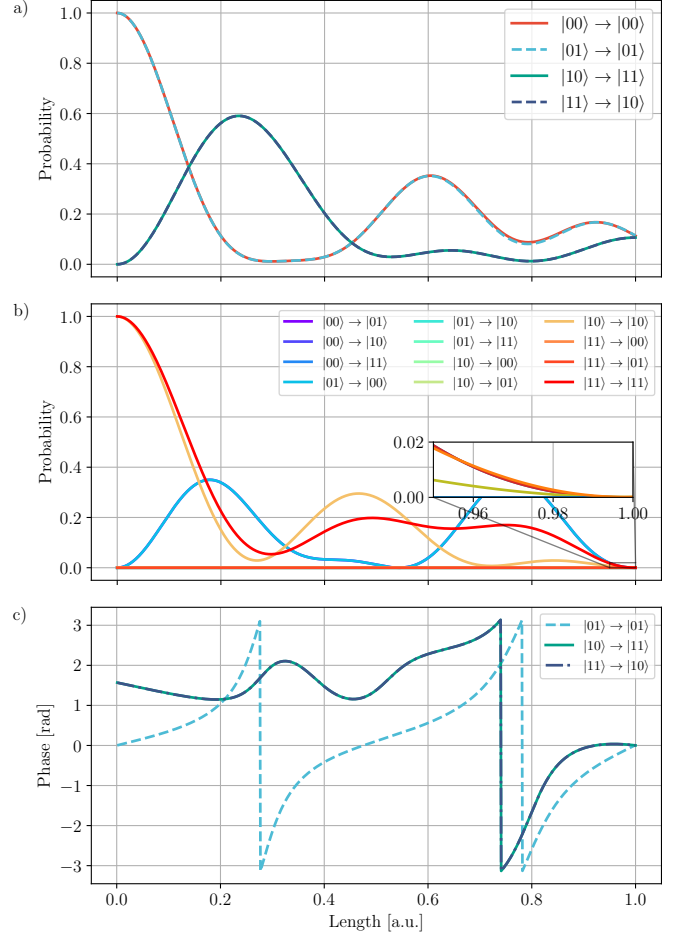


Figure S2. **QW-CNOT evolution.** a) Propagation of the QW-CNOT logical operations. All transfers result in $1/9$ probability. b) Propagation of all other trajectories that would lead to logical errors. All trajectories have zero probability at the end of the evolution. c) Relative phase between the logical states involved in the QW-CNOT operation. The phase of the $|00\rangle$ is set to zero and all relative phases are zero at the end of the evolution, meaning the operation does not induce any additional phase rotations on the logical qubits. Phases stating at $\pi/2$ is equivalent to the phase shift picked up on reflection.

ure S2b. The phase of the CNOT transformations are shown Figure S2c relative to the phase of the $|00\rangle$ state, demonstrating that the QW-CNOT does not add additional phases. The trajectories of each logical input are shown in Figure S3 including the complete Hilbert space.

3. SPDC source

We generate pairs of photons at 1550 nm wavelength in a BBO crystal (Newlight Photonics) pumped with a $\sim 350\text{ mW}$ 775 nm wavelength CW laser (Toptica DL Pro and Newport VAMP). The crystal is designed for type-2 collinear SPDC, meaning the photons are generated

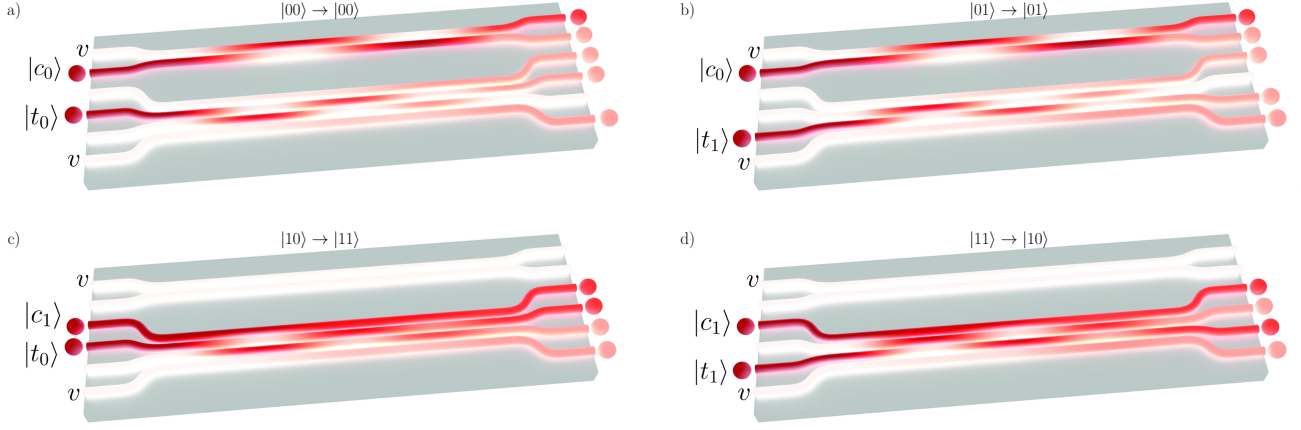


Figure S3. **QW-CNOT gate in the complete Hilbert space.** The trajectories for the two-photon propagation as viewed in the probability distribution of the two photons across the waveguide array. The evolutions include when photons exit the two-qubit subspace. With this plot, it is not possible to see the two-photon correlations that give rise to the CNOT gate.

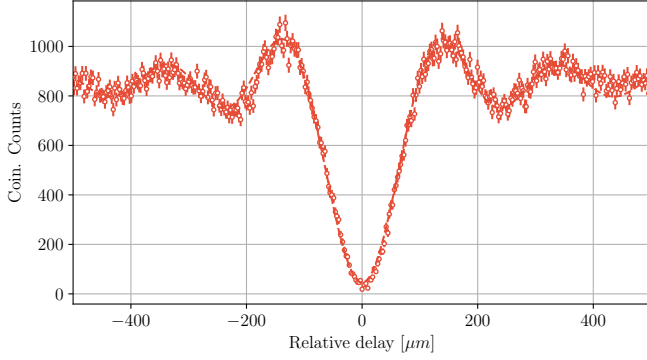


Figure S4. **SPDC Source Indistinguishability.** Hong-Ou-Mandel interference of the photons generated by SPDC. Error bars are calculated using Poissonian statistics.

with orthogonal polarizations. Then we use a 12 nm band pass filter centered at 1550 nm (Thorlabs) to ensure good spectral overlap, and to increase the coherence time of the photons for easier Hong-Ou-Mandel (HOM) interference. The 12 nm filter is also necessary as the Hamiltonian of our device is designed for 1550 nm wavelength and has limited bandwidth. We couple both photons into a single polarization maintaining fiber (PMF) and separate them using a polarizing beam splitter (PBS, OZ Optics). Two optical delay lines (ODLs, OZ Optics) allow for $\sim 1 \mu\text{m}$ precision in the delay length between the two photons before coupling to the chip using v-groove fiber arrays (OZ Optics) with 8° angle from vertical for best grating coupler efficiency. The input and output fiber arrays with $127 \mu\text{m}$ pitch are mounted on 5 axis translation stages (Thorlabs) for positioning and orienting the gratings. Alignment waveguides on either side of the array are used to optimize the alignment such that the waveguide array has close to equal coupling efficiency for all

modes. The collected photons are sent to superconducting nanowire single photon detectors (SNSPDs, Single Quantum) with the polarization optimized for detection efficiency. The electrical signals from the SNSPDs are measured with a time correlator (Swabian Instruments). The SNSPDs have 15 ps to 50 ps jitter and the time correlator 8 ps jitter. A coincidence window of 1 ns is used and the coincidence counts between all four logical outputs of the chip are measured simultaneously. A typical HOM dip from the source, measured with a fused silica beam-splitter (Thorlabs), is shown in Figure S4 with visibility 94.6 %.

4. Two photon measurement and analysis

We measure quantum interference in the QW-CNOT chip by scanning one of the ODLs and measuring the coincidence measurements between the four output channels. We record states that are outside of the logical subspace, however, we do not plot them here for clarity, nor do we measure coincidence in the same output mode via photon number resolving. For the input states $|00\rangle$ and $|01\rangle$, there is no quantum interference in the chip and we simply measure the product of the output probability distributions. However, for the input states $|10\rangle$ and $|11\rangle$, the photons undergo quantum interference and therefore the arrival times must match. Figures S5a and S5b show the experimental and simulated quantum interference for the input $|10\rangle$ state with 900 s integration time for each relative delay. There is quantum interference between the waveguides 3 and 4, which approaches zero when the photons arrive together at the chip. The simulation here is based on the HOM dip in Figure S4 to find the temporal length of the photons. Figures S5c and S5d show the experimental and simulated quantum inter-

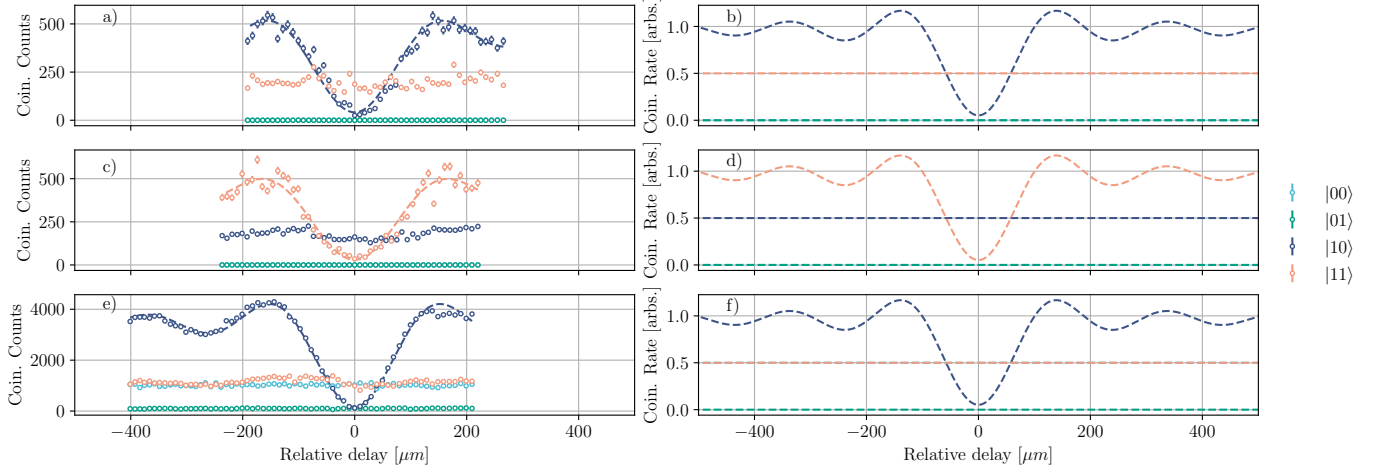


Figure S5. **Quantum interference in the QW-CNOT.** a, b) Experimental and theoretical values for input state $|10\rangle$. The theoretical value of $|11\rangle$ is constant at 0.5, $|01\rangle$ quantum interferes and all others are at 0. c, d) Experimental and theoretical values for input state $|11\rangle$. The theoretical value of $|10\rangle$ is constant at 0.5, $|11\rangle$ quantum interferes and all others are at 0. e, f) Experimental and theoretical values for input state $\frac{1}{\sqrt{2}}(|00\rangle + |10\rangle)$. The theoretical value of $|00\rangle$ and $|11\rangle$ are constant at 0.5, $|10\rangle$ quantum interferes and $|01\rangle$ is at 0. Error bars are calculated using Poissonian statistics.

ference for the input $|11\rangle$ state, where quantum interference now occurs between waveguides 3 and 5. Figures S5e and S5f show the experimental and simulated quantum interference when the input state is in a superposition $\frac{1}{\sqrt{2}}(|0\rangle + e^{i\phi}|1\rangle)$. There is again quantum interference

between waveguides 3 and 5 that approaches zero. This could be the result of the array being in a different position on the chip which can have a slightly different etch depth.